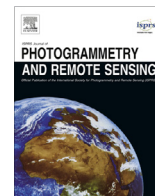


Contents lists available at [ScienceDirect](http://www.sciencedirect.com)

ISPRS Journal of Photogrammetry and Remote Sensing

journal homepage: [www.elsevier.com/locate/isprsjprs](http://www.elsevier.com/locate/isprsjprs)

## Subpixel urban impervious surface mapping: the impact of input Landsat images



Chengbin Deng<sup>a,\*</sup>, Chaojun Li<sup>a</sup>, Zhe Zhu<sup>b</sup>, Weiying Lin<sup>a</sup>, Li Xi<sup>a</sup>

<sup>a</sup> Department of Geography, State University of New York at Binghamton, P.O. Box 6000, Binghamton, NY 13902, United States

<sup>b</sup> Department of Geosciences, Texas Tech University, Lubbock, TX 79409, United States

### ARTICLE INFO

#### Article history:

Received 16 January 2017

Received in revised form 24 June 2017

Accepted 28 September 2017

Available online 14 October 2017

#### Keywords:

Impervious surface  
Random forest  
Atmospheric correction  
Seasonality  
Multi-temporal images  
Landsat

### ABSTRACT

Due to the heterogeneity of urban environments, subpixel urban impervious surface mapping is a challenging task in urban environmental studies. Factors, such as atmospheric correction, climate conditions, seasonal effect, urban settings, substantially affect fractional impervious surface estimation. Their impacts, however, have not been well studied and documented. In this research, we performed direct and comprehensive examinations to explore the impacts of these factors on subpixel estimation when using an effective machine learning technique (Random Forest) and provided solutions to alleviate these influences. Four conclusions can be drawn based on the repeatable experiments in three study areas under different climate conditions (humid continental, tropical monsoon, and Mediterranean climates). First, the performance of subpixel urban impervious surface mapping using top-of-atmosphere (TOA) reflectance imagery is comparable to, and even slightly better than, the surface reflectance imagery provided by U.S. Geological Services in all seasons and in all testing regions. Second, the effect of images with leaf-on/off season varies, and is contingent upon different climate regions. Specifically, humid continental areas may prefer the leaf-on imagery (e.g., summer), while the tropical monsoon and Mediterranean regions seem to favor the fall and winter imagery. Third, the overall estimation performance in the humid continental area is somewhat better than the other regions. Finally, improvements can be achieved by using multi-season imagery, but the increments become less obvious when including more than two seasons. The strategy and results of this research could improve and accommodate regional/national subpixel land cover mapping using Landsat images for large-scale environmental studies.

© 2017 International Society for Photogrammetry and Remote Sensing, Inc. (ISPRS). Published by Elsevier B.V. All rights reserved.

## 1. Introduction

Land cover abundance is defined as the proportion of an area covered by one type of certain terrestrial cover within an image pixel (Shao and Lunetta, 2011; Weng, 2012). A variety of scientific research and practical applications require the information of fractional covers of different types. For example, subpixel impervious surface is an important input in hydrological modeling (Mejía and Moglen, 2010; Zhou et al., 2010), stream hydrology (White and Greer, 2006), water quality analysis (Brabec et al., 2002), urban development monitoring (Jantz et al., 2005; Tsutsumida et al., 2016), urban heat island analysis (Yuan and Bauer, 2007; Deng and Wu, 2013a, 2013b), and socioeconomic analysis (Yu and Wu, 2004; Deng and Wu, 2013c). Percent tree canopy information is

directly associated with biomass, carbon sequestration, stream water temperature, air pollution, fire behaviors, and various forest management practices (Suganuma et al., 2006; Walton, 2008; Coulston et al., 2012, 2013). Shrubland abundance plays an essential role in energy and gas fluxes, regional biodiversity, and global biogeochemical cycles (Thorpe et al., 2013; Xian et al., 2013, 2015). Similarly, due to the nature of high fragmentation and spatial heterogeneity, fractional wetland cover is necessary for accurately mapping important habitats which provides abundant ecosystem services, such as sediment accumulation, water filtering, groundwater recharge, and flood control (United Nations Environment Program, 2010; Reschke and Hüttich, 2014; Huang et al., 2014). Because of the importance and usefulness of subpixel land cover information, several fractional cover products at the global and national scale have been invented and released to the public for applied practices. These well-known products include the 1-km global impervious surface product provided by National Oceanic

\* Corresponding author.

E-mail address: [cdeng@binghamton.edu](mailto:cdeng@binghamton.edu) (C. Deng).

and Atmospheric Administration (NOAA; Elvidge et al., 2007), the 1-km fraction of green vegetation provided by Copernicus Global Land Service (Baret et al., 2013), the 30-m rescaled, 250-m and 500-m global MODIS vegetation continuous fields product (DiMiceli et al., 2011; Sexton et al., 2013), and the 30-m percent imperviousness and tree canopy products of National Land Cover Dataset (NLCD) with a coverage of the contiguous United States (U.S. Geological Service, USGS; Homer et al., 2004, 2007).

In addition to these publicly available products, many methods have been proposed and adapted to derive the fractional cover information of different land cover types in distinct places of the world. These approaches can be grouped into two major categories. The first one is spectral mixture analysis (SMA). Having been developed since 1970s, these SMA methods include classic SMA (Nash and Conel, 1974; Adams et al., 1986; Mustard and Pieters, 1987, 1989), endmember bundling (Bateson et al., 2000), multiple endmember SMA (MESMA; Roberts et al., 1998a; Powell et al., 2007; Franke et al., 2009; Thorp et al., 2013; Deng, 2015; Dengm 2016), spectral weighing (Chang and Ji, 2006; Somers et al., 2009), spectral transformation (Wu, 2004; Zhang et al., 2005, 2006), and spatially adaptive SMA (Deng and Wu, 2013d; Zhang et al., 2015; Shi and Wang, 2014; Wang et al., 2016). The second category is machine learning approaches. These empirical and non-parametric methods include Cubist regression tree (Yang et al., 2003; Deng and Wu, 2013e; Xian et al., 2013, 2015), artificial neural network (Flanagan and Civco, 2001; Weng and Hu, 2008; Hu and Weng, 2009; Shao and Lunetta, 2011), support vector machine (Walton, 2008; Esch et al., 2009; Okujeni et al., 2013), and random forest (Deng and Wu, 2013e; Coulston et al., 2012, 2013; Reschke and Hüttich, 2014; Tsutsumida et al., 2016). These two groups of methods have completely different mechanisms, and therefore, it is difficult to compare the performance of these two methods. A recent study with objective comparisons suggests that these two categories have their own strengths and limitations depending on the availability of training samples: “SMA might be a favorable option with a small number of samples, while Random Forests might be preferred if numerous samples are available” (Deng and Wu, 2013e).

Despite the effectiveness of these methods, many challenges still exist, including the impacts of atmospheric correction, seasonal effect, locational variations (e.g., climate conditions), as well as the usage of multi-temporal images. For example, although the impact of seasonality on mapping urban impervious surface has been examined in the literature, most of the previous studies have an emphasis on two regions. The first region is temperate regions with a humid continental or oceanic climate. Examples include New York (Luo and Mountrakis, 2010; Mountrakis and Luo, 2011), Ohio (Wu and Yuan, 2007; Deng, 2016), Minnesota (Yuan and Bauer, 2007; Deng, 2015), Wisconsin (Yu and Wu, 2004; Deng and Wu, 2013b), Washington (Powell et al., 2008), Connecticut (Flanagan and Civco, 2001), Indiana (Hu and Weng, 2009; Weng et al., 2009), Missouri (Zhou et al., 2012), the Great Lake region (Shao and Lunetta, 2011), Beijing, China (Xiao et al., 2007; Guo et al., 2014), Japan (Yang et al., 2012), Chesapeake Bay watershed (humid subtropical climate; Jantz et al., 2005; Powell et al., 2008; Deng and Wu, 2013e), Wales (oceanic climate; Scott et al., 2014), and Bonn, Germany (oceanic climate; Franke et al., 2009). The second region is the tropical and subtropical areas. Exemplar study areas and climates in the literature include California (Mediterranean climate; Rashed et al., 2003; Roberts et al., 2012; Wetherley et al., 2017), Austin (Sung and Li, 2012), Tampa Bay (humid subtropical climate; Xian et al., 2007), Phoenix (hot desert climate; Myint and Okin, 2009), Brazilian Amazon (tropical monsoon climate; Li et al., 2013), Manaus, Brazil (tropical monsoon climate; Powell et al., 2007), Pearl River Delta, China (subtropical monsoon climate; Zhang et al., 2012, 2016; Fan et al., 2015), and

Jakarta, Indonesia (tropical rainforest climate; Tsutsumida et al., 2016). However, it is still not very clear about the performance of fractional cover estimation in other regions (e.g., Caribbean) with different climate types (e.g., Mediterranean, tropical monsoon and rainforest climate). Also, there is a lack of direct and objective comparison between the estimation performance in different regions, as well as a lack of considering the influence of atmospheric correction. Currently, direct and comprehensive comparisons over various study areas are not feasible to answer these questions. Therefore, taking urban impervious surface abundance as our study target, we have four major objectives in this paper in an attempt to address the aforementioned existing difficulties: (1) exploring how atmospheric correction on Landsat imagery will affect the estimation accuracy of urban impervious surface abundance; (2) examining the impact of seasonality on subpixel urban impervious surface mapping; (3) comparing model performance in study areas with distinct environmental settings in three climates regions; and (4) investigating the estimation performance using a single-date image and multi-season Landsat combinations.

## 2. Study area and data

Three cities with different urban settings located in different climate regions are used as our study area: Binghamton metropolitan area, San Juan metropolitan area, and Los Angeles metropolitan area. Their locations and extents are displayed in Fig. 1. Binghamton metropolitan area is located in Broome County in upstate New York, which represents a humid continental climate with hot summers and cold winters. With a consistently decreasing population since 1970s (dropping from 221 thousand in 1970 to 195 thousand as of 2016 Census ACS), Binghamton is a typical post-industrial shrinking city in the Northeastern United States. Impervious surface areas are mainly found in the downtown area of Binghamton (where the central business district is located), and a number of factories and shopping malls are located separately in the adjacent villages of Endicott and Johnson city, and the main campus of Binghamton University, State University of New York is located in Vestal. To examine the impacts of more spectrally similar land cover categories (e.g., bare soil in croplands and urban impervious surface), the study area includes the entire Broome County. For the second study area, San Juan metropolitan area is in the northeastern coastal areas of the main island of Puerto Rico, which has a tropical monsoon climate. This area is composed of the city of San Juan and its six surrounding municipalities (i.e., cities), including Bayamón, Carolina, Cataño, Guaynabo, Trujillo Alto and Loíza. While they are not constituted as a formal administrative unit, all seven municipalities in this area are economically tied together. This metropolitan area possesses the most populous urban agglomeration in Puerto Rico with approximately 1.25 million residents, which corresponds to a 27% of the total population in this main island. Finally, the third study area is Los Angeles and its adjacent suburban area, which is in Southern California on the West coast of the country. It is the second largest city of the U.S. with a total population over 12 million. This subtropical metropolitan area widely spread out the coastal area, which features a Mediterranean climate with dry summers and moist winters. It is worth noting that, due to the dry and high temperature condition in summers, wildfires always occur in the natural areas close to this study area (such as Santa Monica Mountains and Santa Susana Mountains) in the past few decades (Roberts et al., 1998b, 2003; Riaño et al., 2002; Dennison et al., 2006).

All Landsat images for these three study sites were subset using the boundary shapefiles from U.S. Census Bureau, and re-projected to their respective UTM zone. A total of twelve original Landsat images were used in our experiment. That said, for each study area,

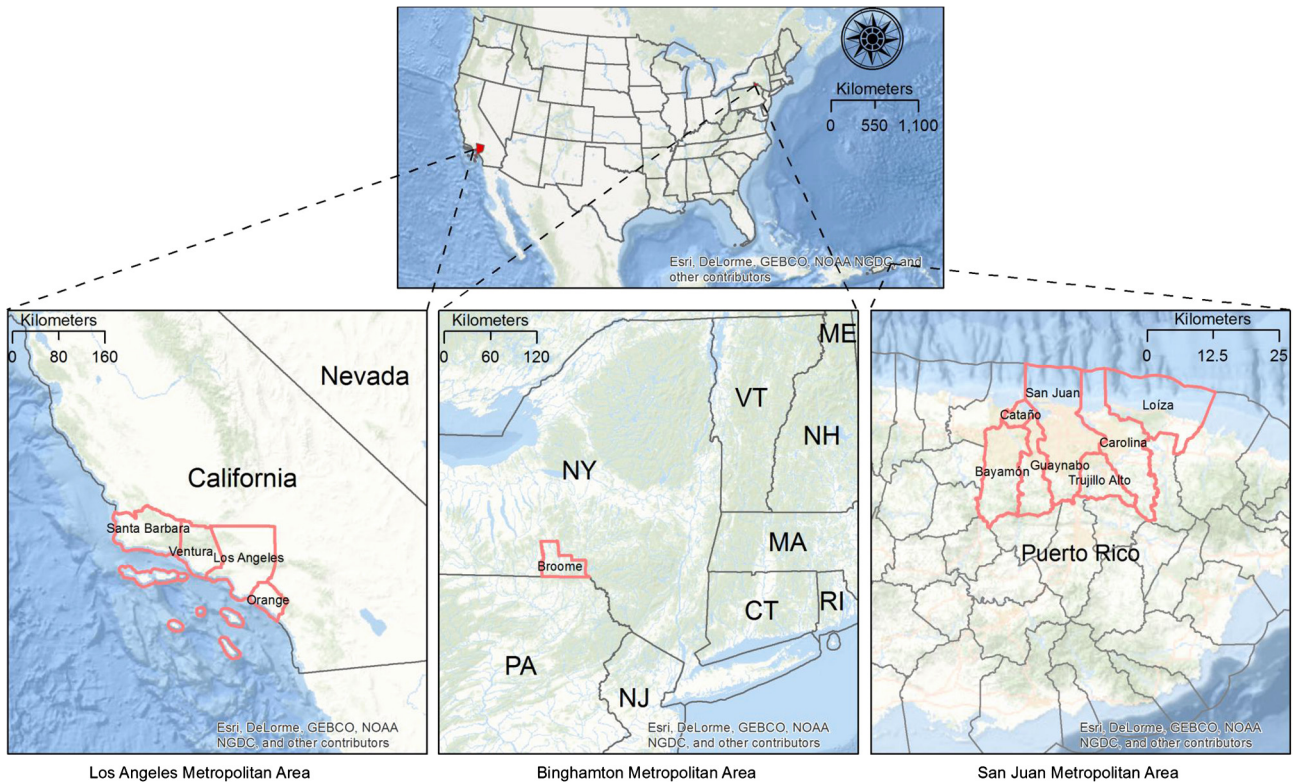


Fig. 1. Study areas of the three metropolitan areas (from left to right): Los Angeles (California), Binghamton (New York), and San Juan (Puerto Rico).

four scenes of original images were directly downloaded from the USGS website. These images correspond to the four different seasons of a year, which represent leaf-on, leaf-off seasons and their transition periods. Among numerous candidate images in the past five years, the image with minimum cloud and snow coverage of each season was selected as a representative image of that season. The information of these images, e.g., the acquisition dates and the percentage of cloud coverage, is shown in Table 1. It is worth noting that Landsat 8 images were employed for all seasons and all study areas except the winter image in Binghamton. Because of the impacts of the lake-effect climate and mountain topography (e.g., valley fog and up-slope fog), it is extremely difficult to find a cloud-free image without snow coverage in winter in the metropolitan Binghamton area. Alternatively, we adopted a Landsat ETM+ image taken in winter 2012 that meets our requirement. Although numerous gaps exist in this Scan Line Corrector (SLC) off image, Binghamton is in the central portion of the Landsat scene and dominated by valid pixels. Therefore, the influence caused by the SLC failure is limited in this study site. These images were then exploited to examine the impacts of seasonal variations on land cover abundance estimation using Random Forest. One image of 1-m orthorectified color aerial photograph was also obtained for each study area to provide ground truth information for training

and testing samples. Note that we selected aerial photographs with an acquisition time that is as close as possible to those of Landsat images. Specifically, the aerial photograph for Binghamton was taken in 2015, Los Angeles in 2016, and San Juan in 2007 (further compared with satellite images from Google Earth), respectively. The process of pixels that experience land cover and land use change during the gap between the acquisition time of the Landsat image and the aerial photograph was detailed in the following section. To consider the topography influence (Homer et al., 2004; Coulston et al., 2013), 30-m ASTER global digital elevation model (DEM) data of each study area was downloaded from the USGS website.

### 3. Methodology

#### 3.1. Image preprocessing

Raw digital numbers (DN) of all Landsat images were first converted to top of atmosphere (TOA) reflectance. These images are called TOA image hereafter. This was done by following the Landsat 7 (Irish, 2000) and Landsat 8 science data user's handbook (USGS, 2016a) by retrieving the image information from the header file of each image (e.g., gain, offset, sun zenith angle, and

Table 1

Landsat images information of the three study areas. All images are Landsat OLI 8 scenes unless specified.

Season	Binghamton		San Juan		Los Angeles	
	Date	Cloud%	Date	Cloud%	Date	Cloud%
Spring	4/24/2014	0.04	5/7/2015	7.37	3/7/2015	0.17
Summer	7/16/2015	0.05	6/10/2016	4.32	8/27/2014	0.16
Fall	11/7/2016	0.11	9/22/2013	1.83	10/19/2016	0.18
Winter	2/6/2012 <sup>a</sup>	0.27	12/30/2014	4.08	2/6/2016	0.38

<sup>a</sup> Landsat ETM+ image.

**Table 2**

Accuracy metrics of three different climate regions using a single-date Landsat image (the best indicator of each assessment category is shaded).

Study Area	Season	Surface Reflectance			TOA Reflectance		
		RMSE	MAE	SE	RMSE	MAE	SE
Binghamton	Spring	9.686	7.075	3.241	9.191	5.329	1.369
	Summer	8.641	5.47	3.225	8.163	4.638	1.387
	Fall	10.999	8.516	5.502	8.423	5.485	2.691
	Winter	11.473	8.282	4.784	10.907	7.824	4.231
San Juan	Spring	12.604	7.827	-1.245	11.623	7.215	-2.438
	Summer	11.952	7.418	-2.196	11.645	7.315	-1.71
	Fall	11.627	7.467	-1.339	10.451	6.484	-1.444
	Winter	10.654	6.606	-1.265	9.374	5.695	-1.004
Los Angeles	Spring	12.406	7.998	3.369	11.506	6.908	3.662
	Summer	12.504	8.757	2.389	11.906	7.131	3.059
	Fall	11.397	7.895	2.444	10.491	6.333	3.226
	Winter	11.586	7.762	2.245	10.659	6.301	3.055

acquisition date). To further test the influence of atmospheric correction, we further derived the USGS Landsat 7 and 8 surface reflectance (SR) data of the same location (hereafter SR images). The Landsat 7 SR images were processed by the Landsat Ecosystem Disturbance Adaptive Processing System (LEDAPS) (Schmidt et al., 2013) and the Landsat 8 SR images were processed by the Landsat 8 Surface Reflectance (L8SR) system (USGS, 2016b). These processes resulted in eight images in each study site for comparison purpose (i.e., two groups of different reflectance types in four seasons). Cloud and cloud shadow were detected by the Fmask algorithm (Zhu and Woodcock, 2012; Zhu et al., 2015). Pixels contaminated by cloud or cloud shadow were then masked out and were not considered in the next steps of model training and validation of the experiments.

### 3.2. Training sample collection

Following a stratified sampling strategy (Deng and Wu, 2013e), we initially generated 400 random samples on the orthorectified aerial photograph in each study site as the training samples of the machine learning model. Half of the random samples were selected from urbanized areas, and the other half were from rural areas. It is worth noting that since not all random samples are valid and used directly, two criteria were set to refine these stratified random samples. First, samples that fall in certain types of land covers or invalid pixels (i.e., water, cloud, and cloud shadow) were automatically removed from both the sample pools. Second, samples that experienced land cover change between 2012 and 2016 (corresponding to the acquisition time of different images of the same study site) were automatically removed as well. This is done by the visual comparison of these samples on the images taken within these years, and the high spatial resolution satellite images from Google Earth, as well as by the local knowledge from the well-trained researchers in our team. In all cases, more than 300 samples remained after the automated removal of those invalid pixels. For comparison purpose, we limited the total sample size to 300 for all study sites. Training samples of percent urban impervious surface was derived by manually digitizing in these 300 original pixels to build the random forest models.

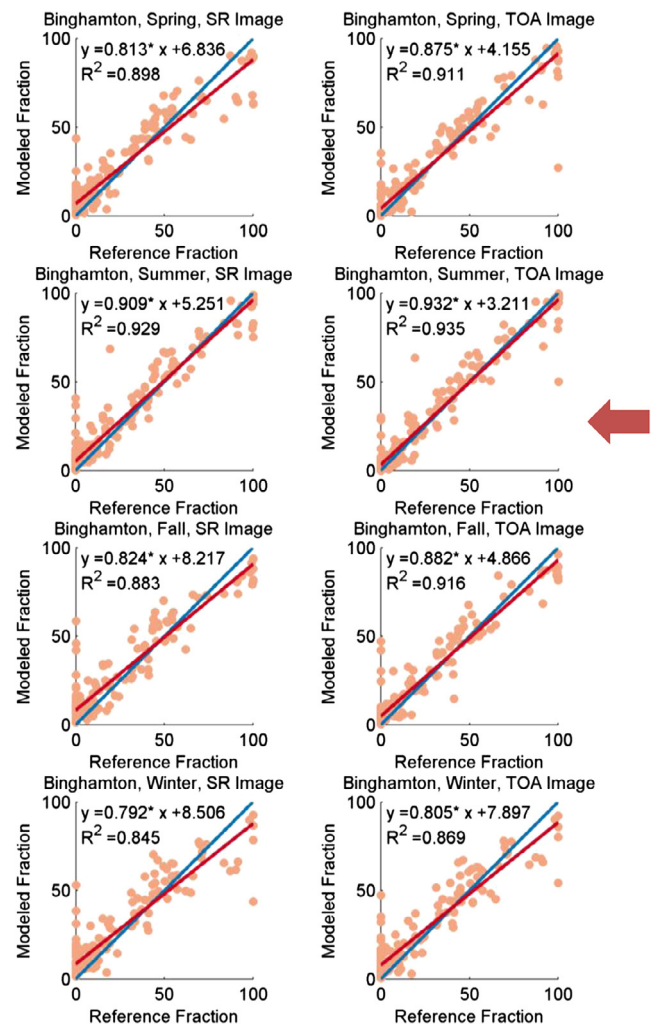


**Fig. 2.** Comparison of a single-date Landsat image with different seasons in Binghamton, New York. The red arrow highlights the scatterplot with the best regression model parameters. (For interpretation of the references to color in this figure legend, the reader is referred to the web version of this article.)

### 3.3. Estimating land cover abundance using random forest

Originally developed for classification and prediction by Breiman (2001), Random Forest is now regarded as one of the most effective machine learning approaches for classifying remote sensing images and deriving fractional land cover information (Deng and Wu, 2013e). The principle of Random Forests is to generate a large number of different regression models for continuous prediction. If a regression tree model is regarded as an individual “tree”, then all the generated models are also compared to a “forest”. A significant feature is that a layer of randomness is implemented to bagging. By using such a mechanism, the approach turns into robust against overfitting (Liaw and Wiener, 2002). Four basic steps are implemented in this non-parametric ensemble algorithm for the prediction of continuous responses (Breiman, 2001):

- (A) Random selection of bootstrap samples from the training pool.
- (B) Random generation of an independent variable subset from all predictor variables.
- (C) Construction of a series of regression tree models by repeating the first two steps.
- (D) Calculation of the mean of the estimates from all built regression tree models as the prediction output.

By following the literature (Yang et al., 2003; Homer et al., 2004; Walton, 2008; Coulston et al., 2013; Xian et al., 2013), the SR and TOA reflectance of all optical Landsat bands of a single-date image (or a combination of seasonal images) and the ASTER DEM were used as the independent variables to construct the empirical random forest model in each study area.

### 3.4. Accuracy assessment

A total of 300 testing sample polygons were used in each study site for accuracy assessment. They were also randomly selected based on a stratified sampling strategy (Deng and Wu, 2013e). This strategy is the exact same as that of training data sampling as mentioned earlier, but with completely different sample pixels. No cloud-contaminated or cloud shadow-contaminated pixel is included in any testing sample polygon. Based on the previous studies (Powell et al., 2007; Deng and Wu, 2013d; Deng, 2016), each sample covers a geographical area of 90 by 90 m (i.e., a 3 by 3 Landsat pixel neighborhood). In each testing polygon, reference information was derived by manually digitizing all urban impervious surfaces on the orthorectified photograph. The percent impervious surface as ground truth was then calculated as the overall geographical area of digitized impervious surface divided by the area of a testing polygon (i.e., 8100 m<sup>2</sup>). Three widely used assessment indicators, including root mean square error (RMSE), mean

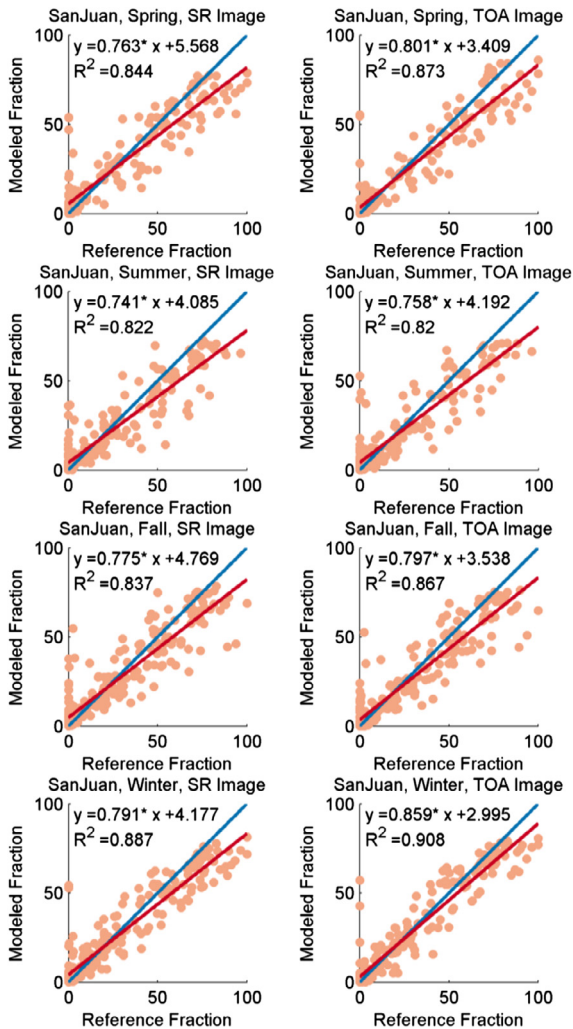


Fig. 3. Comparison of a single-date Landsat image with different seasons in San Juan, Puerto Rico.

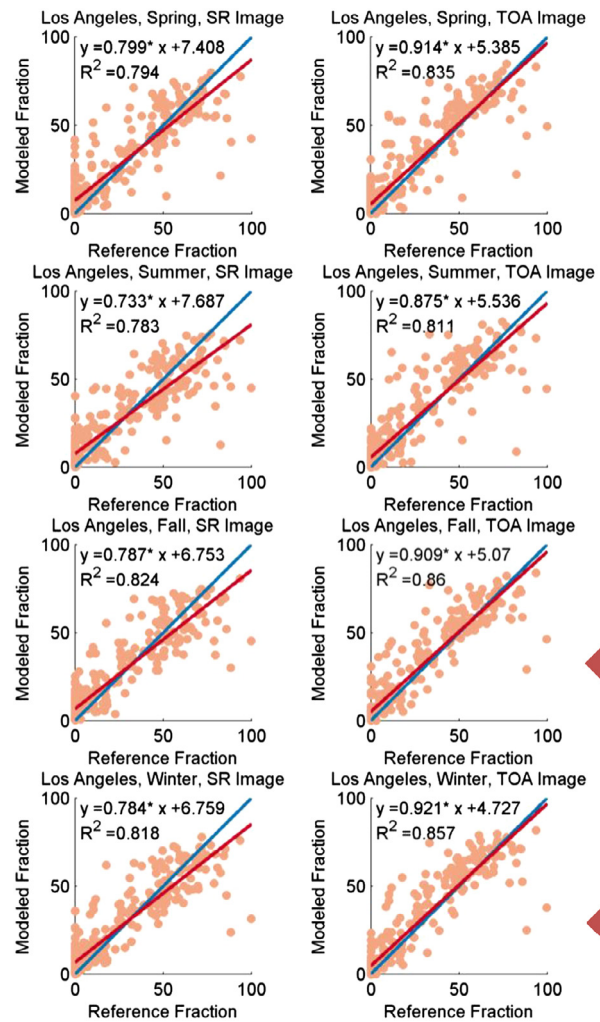


Fig. 4. Comparison of a single-date Landsat image with different seasons in Los Angeles, California.

absolute error (MAE), and systematic error (SE), were calculated to evaluate the model performance of all seasonal images in each study area (Powell et al., 2007; Deng, 2015, 2016). The first two indicators are calculated to quantify the estimation accuracy, while the last indicator is adopted to measure the overall estimation trend or bias in the entire study area. If there are smaller values for RMSE and MAE, it indicates that the fractional cover estimation is more accurate. If a smaller number is found with SE, it suggests a small bias in the estimation. The formulae of these three metrics can be expressed as follows.

$$\gamma = \sqrt{\frac{1}{n} \sum_{i=1}^n (\hat{f}_i - f_i)^2} \tag{1}$$

$$\mu = \frac{1}{n} \sum_{i=1}^n |\hat{f}_i - f_i| \tag{2}$$

$$\delta = \frac{1}{n} \sum_{i=1}^n (\hat{f}_i - f_i) \tag{3}$$

where  $\gamma$  is RMSE;  $\mu$  is MAE;  $\delta$  is SE;  $\hat{f}_i$  is the estimated abundance of urban impervious surface of sample  $i$  using random forest;  $f_i$  is the digitized impervious surface abundance of sample  $i$  from the aerial photographs; and  $n$  is the total of all sample polygons. Moreover, scatterplots of the predicted urban impervious surface using random forest were also plotted against the digitized ground-truth samples from the orthorectified aerial photographs.

## 4. Results

### 4.1. Results using a single-date image

The three accuracy metrics were calculated and reported in Table 2. Scatterplots are drawn and shown in Figs. 2–4. In these figures, regression model between the modeled and actual urban impervious surface fractions of each scatterplot is built. The regression line is shown in red, while the 1:1 reference line is shown in blue. The slope, intercept and coefficient of determination (i.e., R-squared) of the regression model were calculated and displayed in each figure. For better visual comparisons of the performance of different seasons, the scatterplots using SR images are displayed in the first column of each figure, while those using TOA reflectance images are illustrated in the second column. In each figure, row one to four correspond to spring, summer, fall and winter images, respectively.

For Binghamton area, two observations are noticed in the upper panel in Table 2. First, quantitative indicators in the last three columns on the right are better than their counterparts in the first three columns on the left. This indicates that the performance of the TOA reflectance images is as good as, and even slightly better than, the SR images in all seasons. Second, the best accuracy indicators with minimum values are found in the summer image (with an RMSE of 8.16%, and an MAE of 4.64%), followed by spring and fall images, and the least accurate estimation is associated with the winter image. This trend is the same for both SR and TOA images. Similarly, as shown in Fig. 2, scatterplots of all the four seasons looks acceptable: other than a small number of outliers, most of the scatterplots cluster around the red 1:1 reference line.

**Table 3**  
Accuracy metrics of three different climate regions with different seasonal combinations using two Landsat images (the best indicator of each assessment category is shaded).

Locations	Season Combination				SR			TOA		
	Spring	Summer	Fall	Winter	RMSE	MAE	SE	RMSE	MAE	SE
Binghamton	×	×			8.665	5.410	-2.728	8.006	4.426	-1.606
	×		×		8.905	6.288	-3.409	6.906	4.485	-1.930
	×			×	9.608	6.792	-3.244	7.508	5.017	-1.836
		×	×		8.799	5.619	-3.662	7.393	4.598	-2.524
		×		×	9.050	5.927	-3.679	7.381	4.782	-2.517
			×	×	9.967	7.159	-4.458	8.194	5.625	-2.639
San Juan	×	×			11.420	7.829	2.493	10.772	6.943	3.277
	×		×		11.424	7.470	2.501	10.163	6.630	2.837
	×			×	10.465	6.770	0.837	9.977	6.163	0.605
		×	×		10.623	7.163	2.085	9.810	6.639	2.047
		×		×	9.468	6.207	1.246	8.550	5.729	1.327
			×	×	9.115	6.002	0.495	7.832	4.975	0.423
Los Angeles	×	×			12.098	7.972	3.417	11.587	7.118	4.040
	×		×		11.871	7.823	3.563	11.250	6.884	3.648
	×			×	11.995	7.821	2.938	10.975	6.739	3.704
		×	×		11.656	8.136	2.193	10.333	6.441	3.195
		×		×	11.580	8.213	2.722	10.654	6.569	3.364
			×	×	11.620	7.920	2.575	10.652	6.425	3.485

Moreover, all the slopes of the regression lines are greater than 0.8, their intercepts are less than 8%, and the coefficients of determination are better than 0.86. With the smallest intercept (3.21), and the greatest values of slope (0.93) and R-squared (0.94), the performance of the summer image outperform image of any other season. This further confirms the observation from the findings in this humid continental climate zone.

For San Juan area, it is observed that the performances of TOA reflectance images on the right portion are consistently better than those of SR images on the left portion. Almost all metrics of TOA images is approximately 1% better than those of SR images. Comparatively, the central panel of Table 2 reveals that the seasonal trend in San Juan is opposite to that in Binghamton. In this tropical monsoon region, the best accuracy indicators are found in the winter image with an RMSE of 9.37%, an MAE of 5.7%, and an SE of -1%, followed by fall and spring. The least satisfactory metrics are found with the summer image. In the regression model in Fig. 3, the performances of all images seem adequate: all R-squared values greater than 0.82, slopes higher than 0.75, and intercepts less than 5%. Highest correlations in the TOA winter image can be clearly discerned, generating the greatest values of R-squared (0.91), the highest slope (0.86) and the smallest intercept (3.0). This suggests that winter image has the optimal performance among images of all four seasons in this tropical monsoon area.

For Los Angeles area, the overall result is similar to that in San Juan. First, by examining the lower panel of Table 2, the accuracy metrics of the TOA images remain superior to those of the SR images. Second, the best RMSE (10.49%) is with the TOA fall image; the best MAE (6.3%) is from the TOA winter image; and the best SE

(2.25%) is from the SR winter image. The poorest performance is from the summer image. Scatterplots in Fig. 4 also confirm such observations. The fall image has the highest R-squared value (0.86), while the winter image possesses the most close-to-one slope (0.92) and the least intercept (4.73%) among the four seasons. Overall, the performances of the TOA fall and winter images are comparable with each other, and the difference between them is very small.

4.2. Results of seasonal combinations with two images

For the experiments with seasonal combinations using two images, a total of six combinations of different seasons were tested for each study site. Their accuracy indicators are reported in Table 3, and their scatterplots are displayed in Figs. 5–7 for three study areas. In these figures, the first column is scatterplots using SR images, while the second column is corresponding to the same seasonal combination but using TOA reflectance images. This relationship also applies to the third and fourth columns, respectively. Similar to the experiments using single-date images, it is not surprising to find that all TOA images are as good as, and even outperform, their counterparts of SR images in three study areas. For Binghamton area, the best accuracy metrics in Table 3 are associated with the TOA summer and spring combination, and the TOA fall and spring combination. In Fig. 5, almost all regression models have very decent model parameters, as supported by a near 1:1 relationship, with a close-to-one slope (all greater than 0.88) and a near-to-zero intercept (all less than 7%). Among them, the least intercept is found with the combination of TOA summer and spring

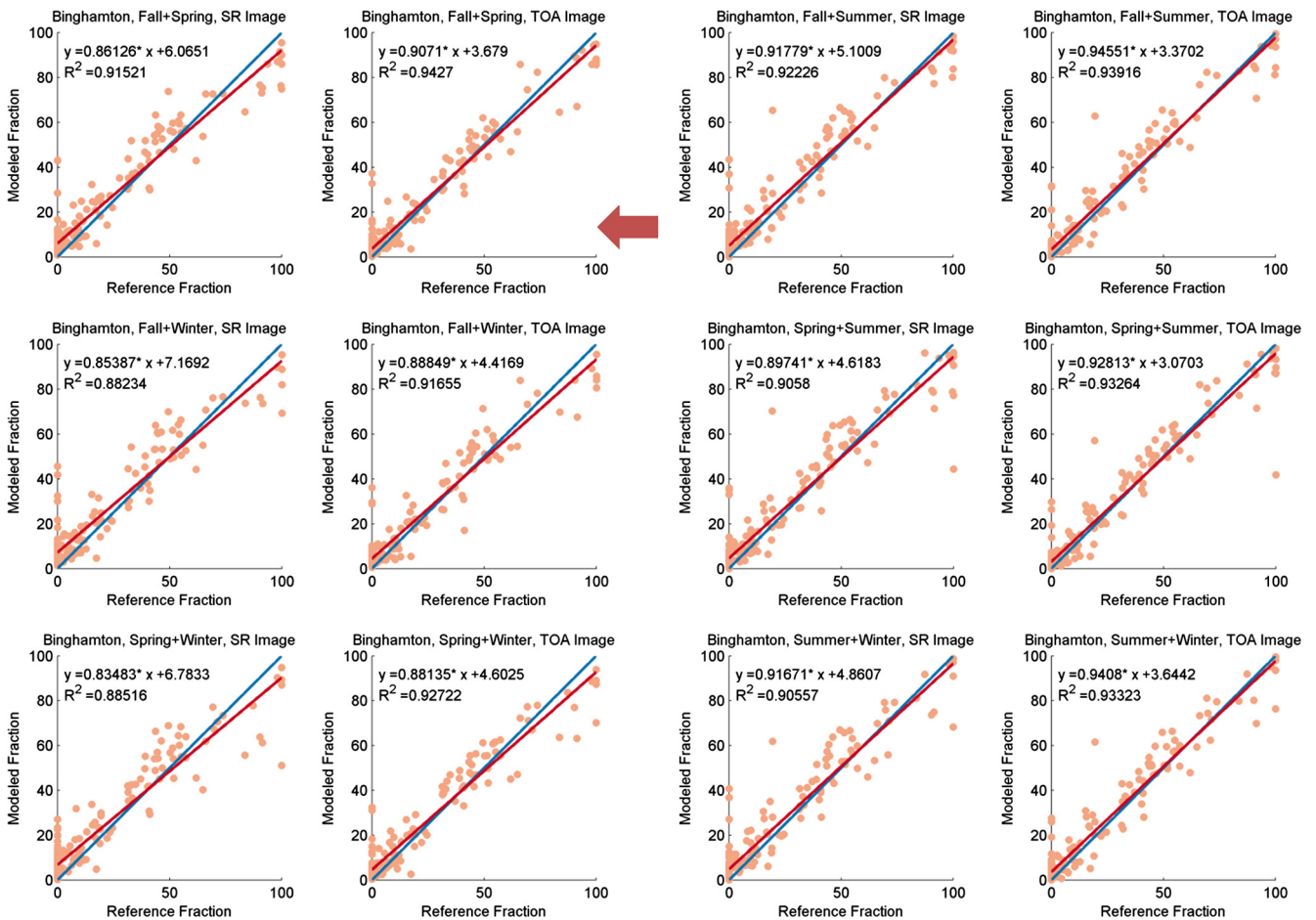


Fig. 5. Comparison of different seasonal combinations using two Landsat images in Binghamton, New York.

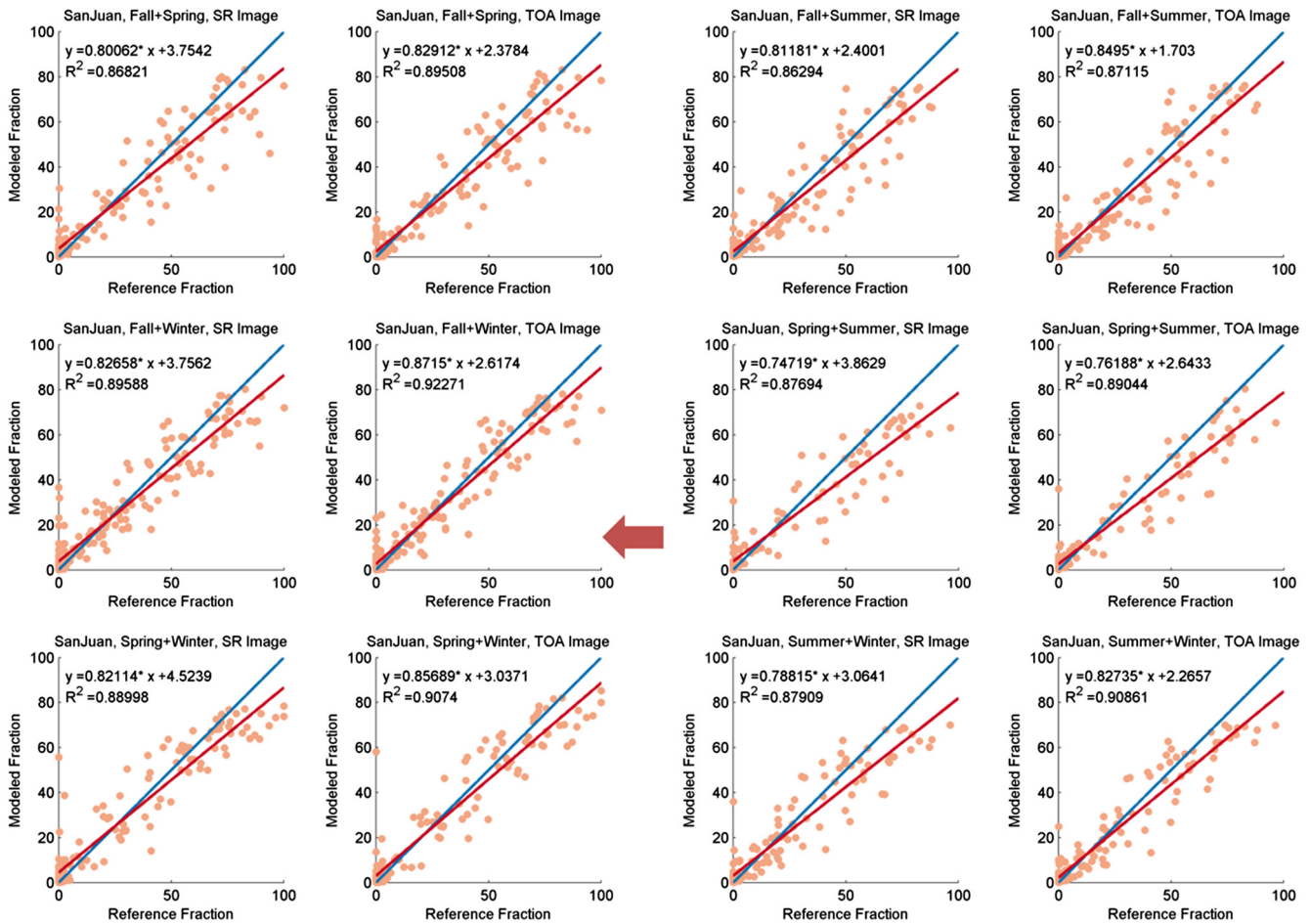


Fig. 6. Comparison of different seasonal combinations using two Landsat images in San Juan, Puerto Rico.

images (3.07%), and the greatest slope is found with the TOA fall and spring combination (0.95). For San Juan area, similar to the analysis in the usage of single-date image, the performance of TOA fall and winter combination does not vary much with, and slightly outperforms, that of any other combination with an RMSE of 7.83%, an MAE of 4.98%, and an SE of 0.42. The scatterplots in Fig. 6 also confirm this observation. The best parameters among the regression models are from the scatterplot of the TOA fall and winter combination, producing greatest R-squared (0.92), and the highest slope (0.87). For Los Angeles area, there is no obvious variation among the performance of all seasonal combinations (see the lower panel in Table 3). This is also similar in the single-date image comparison. The best accuracy metrics can be found in the TOA fall and winter combination and the TOA fall and summer combination. In Fig. 7, the metrics and scatterplots of these two combinations also have the similarly favorable parameters among others: an RMSE of 0.86, the highest slope of 0.9, and the smallest intercept of 5.1%.

4.3. Results of seasonal combinations with three scenes and more

The performances of the combinations of multiple seasons (three or more) were quantified in Table 4, and their scatterplots were drawn in Figs. 8–10. A total of five combinations were tested for each study area, i.e., four combinations of any three seasons and one that includes all four seasons. For Binghamton area, while visual examination in Fig. 8 finds that all scatters are lying close to the 1:1 reference line, the combination of TOA spring, summer, and fall generates the most accurate result among all combinations

with an RMSE of 6.76%, an MAE of 4.26% in the upper panel of Table 4. This is further confirmed by the regression model parameters: an R-squared of 0.95, a slope of 0.95, and an intercept of 3.02%. It is followed by the combination of TOA spring, summer, and winter. This may reveal that the inclusion of spring and summer, the two most accurate images in the single-date image group, will produce the best performance. On the contrary, the inclusion of the winter image always leads to an unsatisfactory result (e.g., the poorest combination is found with the one collectively using winter, summer and fall images).

For San Juan area, the optimal accuracy metrics in the central panel of Table 4 is produced by the combination of TOA winter, fall, and summer images. However, the combination of TOA winter, fall, and spring images and the combination of all seasons do not vary much with it. Similar observations can be found in Fig. 9. The smallest intercept (1%) is related to the combination of all four seasons, the highest slope (0.88) and the greatest R-squared (0.93) is from the combination of spring, fall, and winter images. This may suggest that the inclusion of winter images can effectively improve the estimation accuracy, which is opposite to the experiments of Binghamton area.

For Los Angeles area, the shaded metrics (with an RMSE of 10.59% and an MAE of 6.5%) in the lower panel in Table 4 is the minimum errors among all combinations, which corresponds to the combination of TOA winter, fall, and summer images. This observation is consistent with the scatterplots in Fig. 10, where this combination possesses a slope of 0.86, a slope of 0.91, and an intercept of 5.29%. In terms of using all four season images in the three study areas, although their performances are acceptable, they

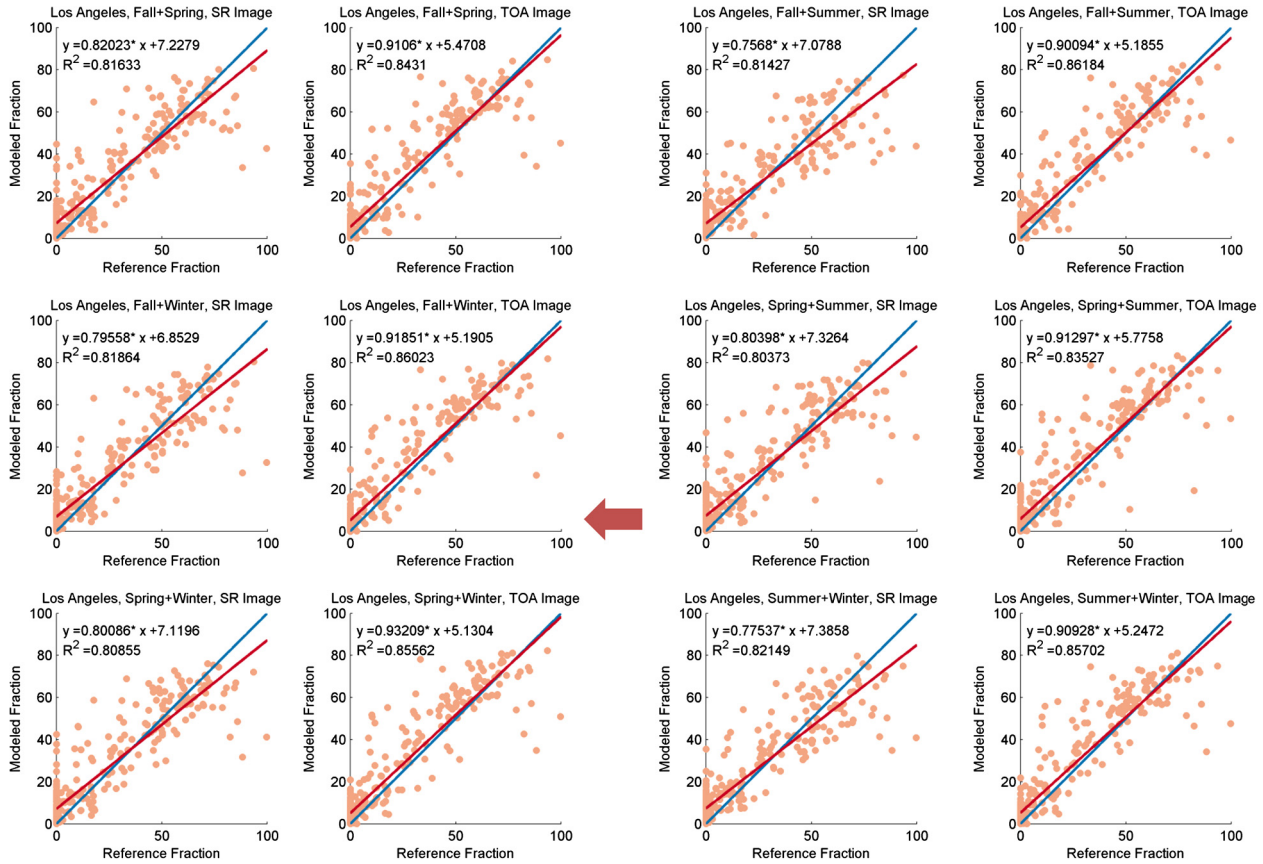


Fig. 7. Comparison of different seasonal combinations using two Landsat images in Los Angeles, California.

Table 4

Accuracy metrics of three different climate regions with different seasonal combinations using three or more Landsat images (the best indicator of each assessment category is shaded).

Locations	Season Combination				SR			TOA		
	Spring	Summer	Fall	Winter	RMSE	MAE	SE	RMSE	MAE	SE
Binghamton	×		×	×	9.001	6.534	3.798	7.265	4.712	1.783
	×	×	×		8.261	5.261	3.047	6.757	4.257	2.155
	×	×		×	8.711	5.577	3.255	6.859	4.324	1.890
	×		×	×	8.867	5.685	3.524	7.510	4.679	2.316
San Juan	×	×	×	×	8.706	5.545	3.078	6.966	4.541	2.262
	×		×	×	9.237	6.458	-0.471	8.262	5.631	-1.322
	×	×	×		10.855	6.703	-3.928	10.712	6.593	-4.107
	×		×	×	10.026	6.841	-2.350	8.873	5.582	-2.218
Los Angeles	×		×	×	8.855	6.036	-1.144	8.165	5.427	-1.185
	×	×	×	×	8.649	5.709	-1.733	8.237	5.052	-1.909
	×		×	×	12.015	7.796	3.265	11.034	6.795	3.388
	×	×	×		11.904	7.839	3.510	10.761	6.607	3.622
Los Angeles	×	×		×	11.508	7.686	2.762	11.236	6.975	3.665
	×		×	×	11.804	8.162	2.857	10.588	6.501	3.479
	×	×	×	×	11.720	7.790	3.501	11.071	6.865	3.840

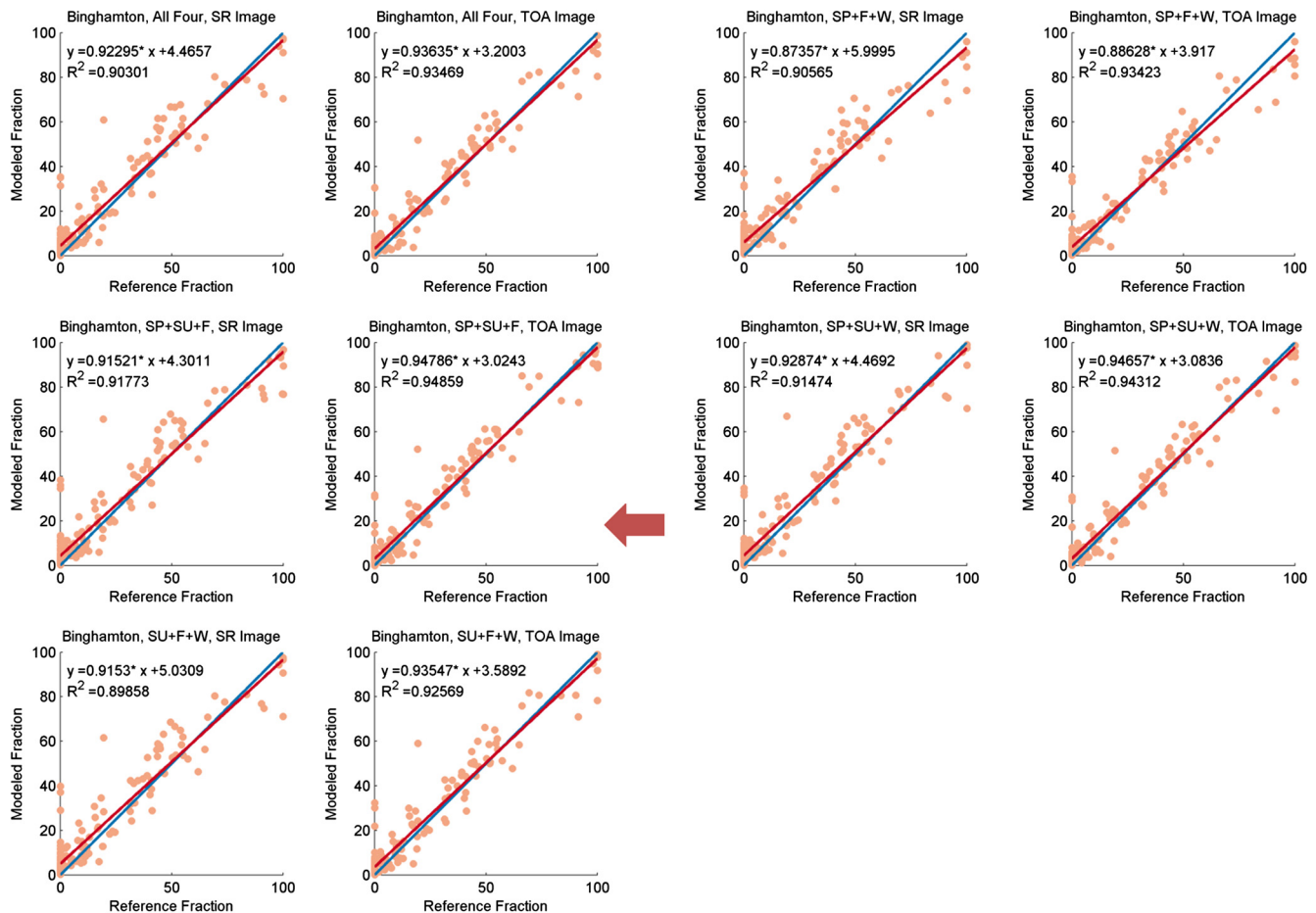


Fig. 8. Comparison of different seasonal combinations using three or more Landsat images in Binghamton, New York.

might not be the optimal combination in the multiple seasonal tests, and is as not as good as one of the three-image combination.

## 5. Discussions

### 5.1. Comparison between the performance using surface reflectance and TOA reflectance images

One of the interesting findings from our experiments is that the performances of the TOA reflectance images are consistently comparable to, and even slightly better than, those of the SR images in all experiments. Such finding is observed not only in the temperate area with humid continental climate, but also in the subtropical and tropical areas with monsoon and Mediterranean climates. This is mainly because the training data for our experiments are directly collected from and applied to the same Landsat image for subpixel urban impervious surface mapping. That said, the classifier has already been well-trained by the current atmospheric condition of the same images provided by the training data. As long as the atmospheric condition is homogenous within the image (for example, aerosol optical thickness is similar), atmospheric correction may not be necessary. Especially in this study, the requirement of homogeneous atmospheric condition was met in all study areas, since images with minimum cloud coverage (close to zero) were employed. Note that this is different from the use of transferable samples from images of the same area but taken on other dates or from images acquired at other locations. In these two cases when atmospheric condition is not the same, atmospheric correction is recommended. This explanation is also supported by the

work of Song et al. (2001). Moreover, both the LEDAPS and L8SR algorithms may not be perfect, and the Landsat 8 surface reflectance products are only provisional at the moment. Recent studies have reported inconsistency in surface reflectance between Landsat 8 and the previous Landsat sensors (Zhu et al., 2016; Holden and Woodcock, 2016; Roy et al., 2016). Therefore, the artifacts of the atmospheric correction algorithm are likely to be introduced into the corresponding surface reflectance products, and may further reduce the classification accuracies. Further studies are needed in the future to examine the effects of different atmospheric correction methods on fractional land cover estimation, as well as to improve atmospheric correction for Landsat 8 images.

### 5.2. Seasonal effects

Summer images have been widely used in most existing studies. This might be because that the leaf-on images are easier to obtain due to the greater chance of cloud-free days in summer (such as in Midwest in the U.S. in the works of Weng et al., 2009; Deng, 2015, 2016), while both cloud and snow are often captured in the winter images. How imagery of other seasons affect the estimation accuracy in different climate regions is still not well studied in the literature. According to the comprehensive comparisons and analyses in our research, seasons that can reach the best estimation accuracy of urban impervious surface are identified in the three study areas. First, for temperate regions with a humid continental climate, the experiment results of Binghamton indicate that the performance of the summer image is better than the winter image. This is primarily because most vegetation in this climate

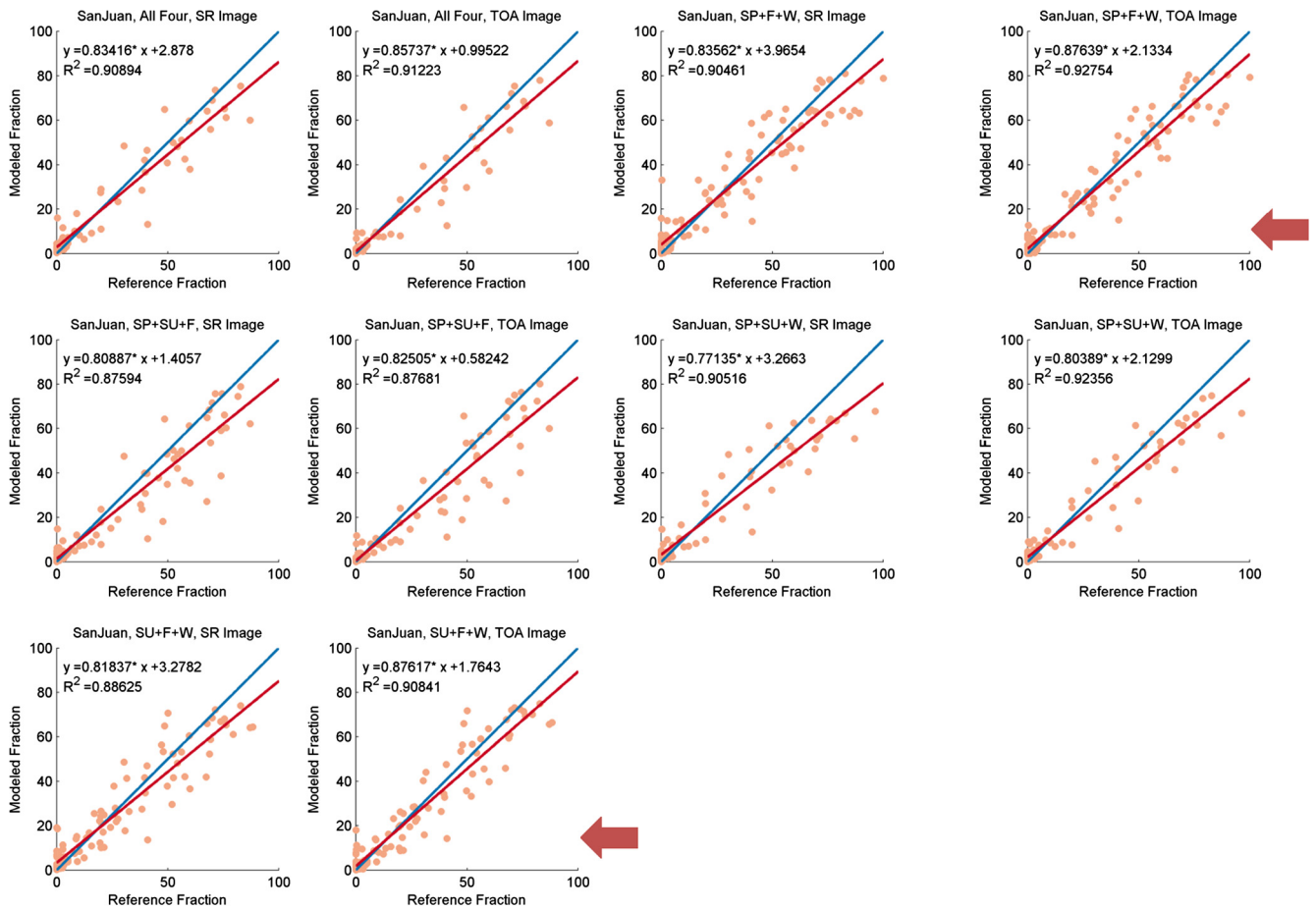


Fig. 9. Comparison of different seasonal combinations using three or more Landsat images in San Juan, Puerto Rico.

region is senescent in winter, and accordingly bare soil and tree trunks are exposed. These land covers are spectrally similar with dark urban impervious surface, such as asphalt and tar. By contrast, when leaves reach its peak in summer, bare soil and tree trunk are likely to be covered by tree canopy, which significantly reduces the spectral confusion. Such seasonal variations in Binghamton in summer and winter can be clearly seen in Fig. 11A and B, respectively. This explanation of plant phenology is also supported by the literature with study areas in the same climate zone (Wu and Yuan, 2007; Weng et al., 2009). In the case of multi-temporal combination (using two and more seasons) in this region, the performance of the combinations with the summer image is constantly better than the combination with the winter image when controlling for image scenes of other seasons.

For regions with a tropical monsoon climate or a Mediterranean climate, the experiment results in San Juan and Los Angeles suggest that the performance of fall and winter images is consistently better than spring and summer. While the conclusion seems the same for both locations, the causes could be different from each other. In San Juan, wet season usually ranges from April to November. Dense vegetation, therefore, is always associated with the abundant moisture in the wet and hot summers, which could affect the estimation of fractional impervious surface (Zhang et al., 2014, 2016). Due to the spectral similarity between water and dark impervious surface, water may be mistaken as impervious surface in some natural landscapes (e.g., wetlands) as urban impervious surface when using summer images. In the dry season with less water content in winter in San Juan, such spectral confusion is likely to be less severe and the influence on impervious surface esti-

mation be less apparent. By contrast, summer is usually dry and hot in Los Angeles, and precipitation occurs mainly in winters with mild temperature. Thus, quite a few bare soil and non-photosynthesis vegetation (NPV) are exposed in summers, while they are heavily covered by growing vegetation in mild and moist winters. Such seasonal change of land covers in Los Angeles in summer and winter can be apparently discerned in Fig. 11C and D, respectively. Therefore, the preference of winter images in tropical monsoon and subtropical Mediterranean climates supplements the existing literature in which summer images used to be suggested and widely used.

### 5.3. Performance with different environmental and urban settings

An effort in our research is to perform direct and objective comparisons on fractional impervious surface estimation with different environmental settings under different climate conditions. For temperate regions with a humid continental climate, the Binghamton analysis shows that, even using a single-date image, our results based on random forest can achieve a satisfactory level with an RMSE of 8.26%, an MAE of 4.64%, and an SE of 1.39%. This is slightly better than the indicators described in Wu and Yuan (2007; with an RMSE of 10.22%, and an SE of  $-4.32\%$  in Ohio), Hu and Weng (2009; with an RMSE of 11.8%, and an MAE of 8% in Indiana), Weng et al. (2009; with an RMSE of 13.2%, an MAE of 8.7% in Indiana), and Deng (2016; with an RMSE of 13.94%, an MAE of 10.13%, and an SE of  $-2.56\%$  in Ohio). For tropical and subtropical regions with a monsoon climate, similar better results can be observed in San Juan: a favorable level can be reached with an RMSE of

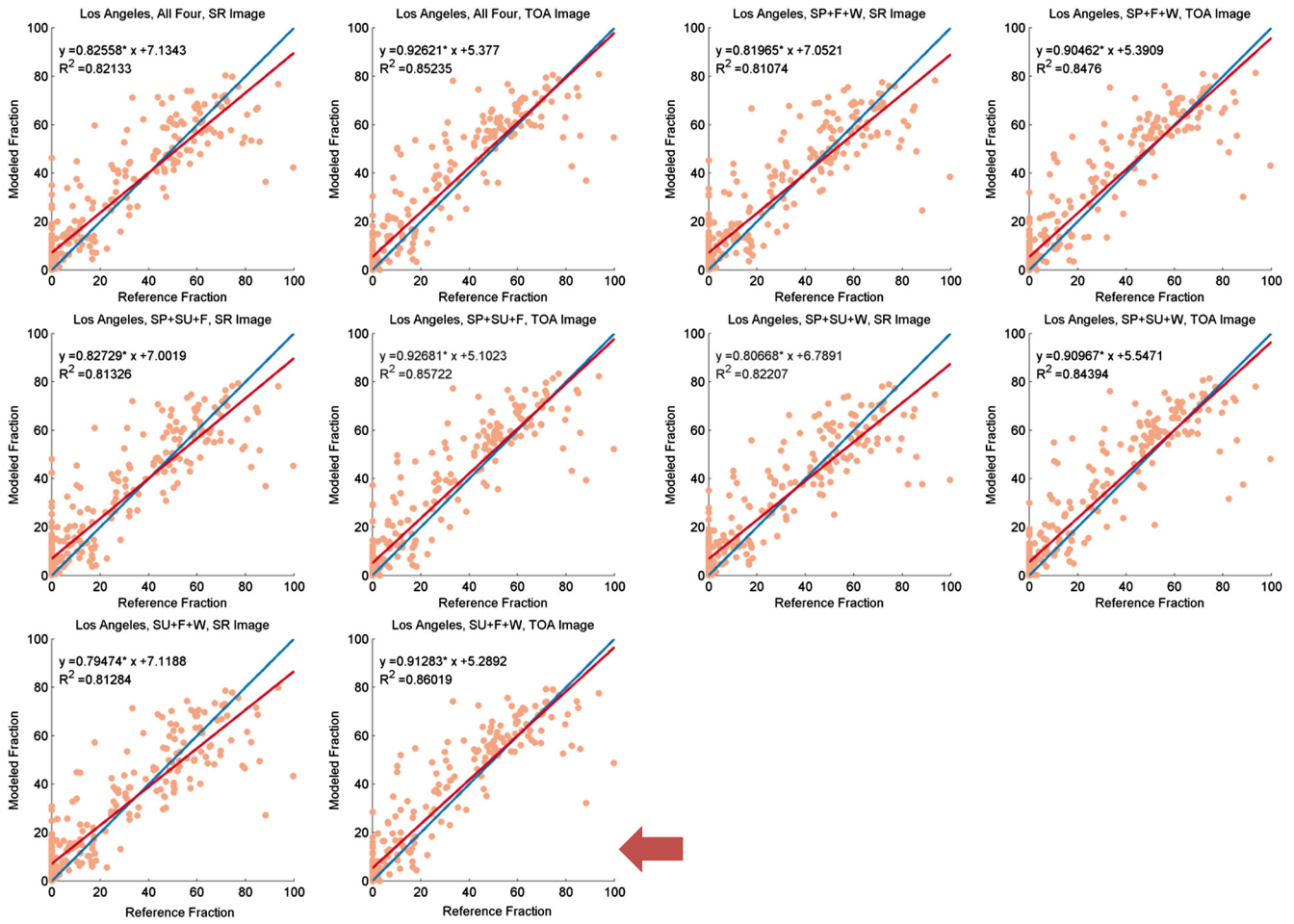


Fig. 10. Comparison of different seasonal combinations using three or more Landsat images in Los Angeles, California.

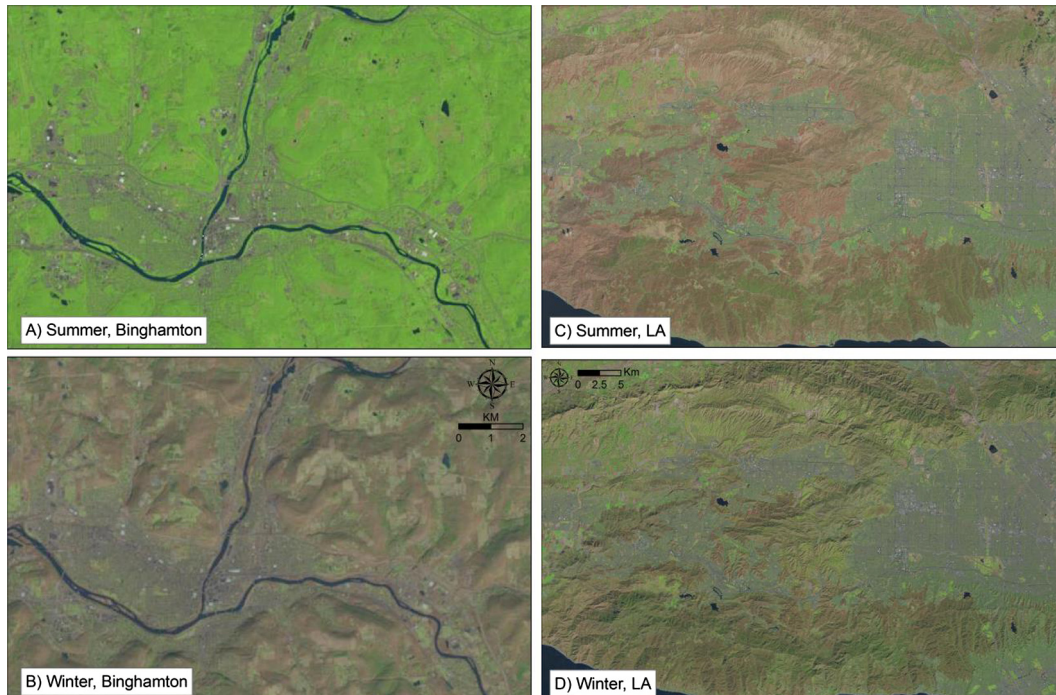


Fig. 11. Comparison of different seasons in two study areas using natural color composites. The first row shows the summer images, and the second row shows the winter images. The first column is Binghamton, New York, and the second column is Los Angeles, California.

9.37%, an MAE of 5.7%, and an SE of  $-1\%$ . These results somewhat outperform the estimation metrics reported in other studies under a similar monsoon climate, such as Powell et al. (2007; with an MAE of 13.8% and an SE of 5.2% in Manaus, Brazil), Li et al. (2013; with an RMSE of 15% in Brazilian Amazon), Fan et al. (2015; with an RMSE of 10%, an MAE of 8.6%, and an SE of 7.8% in Guangzhou, China), and Tsutsumida et al. (2016; with an RMSE of 16.39% in Jakarta, Indonesia). For subtropical regions with a Mediterranean climate, our results in this study are slightly better than other studies as well, in which a slope of 0.91, an intercept of 5.1, a coefficient of determination of 0.86, an RMSE of 10.6%, an MAE of 6.3% and an SE of 3.1% are achieved. Comparatively, under the same climate condition, the value of R-squared reported in Roberts et al. (2012) is 0.79 at 15-m resolution and 0.72 at 60-m resolution, respectively. The slope in their work is 1.432 at 15-m resolution and 1.443 at 60-m resolution, while the intercept is 7.7% at 15-m resolution and 11% at 60-m resolution. All these comparisons may be explained by the findings in previous studies that machine learning methods tend to have a better performance than SMA approaches when a large sample size is available (Deng and Wu, 2013e; Belgiu and Drăguț, 2016). By comparing the results in our experiments with various combinations, the temperate region with a continental climate has consistently better performances than the other two regions. Although direct and comprehensive comparisons have been performed in this research, more studies in other locations with various climate conditions are warranted in the future to fully understand the performance of fractional cover estimation using machine learning methods.

#### 5.4. The impacts of multi-season scene combinations

In addition to examining the seasonal effect using a single-date image, we also investigated whether the inclusion of as many multi-temporal images as possible can enhance the accuracy of fractional impervious surface estimation. When compared the performance of using a single-date image with multi-season combinations, it can be found that the improvement of estimation accuracy displays a similar trend of improvement in both Binghamton and San Juan. The accuracy metrics in Tables 2 and 3 show that, in Binghamton and San Juan, an RMSE increment of approximately 1.5% can be reached by using two TOA images when compared with a single-date image. Comparatively, the performances in Los Angeles are relatively stable, and the accuracy indicators have no obvious increase or decrease (also see Tables 2 and 3). However, when more than two multi-season images were collectively used (i.e., the combinations of three and four images of different seasons), the increment still exists, but it is as low as 0.2% and is almost negligible. Our finding is similar to and confirms that of Coulston et al. (2013). Namely, more data may not significantly increase the performance of empirical machine learning models, and the use of parsimonious number of images may be sufficient for fractional land cover mapping, especially when using machine learning approaches.

## 6. Conclusions

Urban impervious surface information is of great necessity in a variety of urban analyses. Because of the mixed nature of satellite imagery, subpixel urban impervious surface product provides more information than per-pixel classification (Zhang et al., 2012, 2014). Subpixel urban impervious surface mapping is challenging due to the heterogeneity of urban environments (Weng et al., 2009; Deng, 2016). During such mapping process, factors that affect the accuracy of subpixel cover estimation include atmospheric correction, climate conditions, seasonal effect, and urban settings. These

factors, however, have not been well studied. This research performed direct and comprehensive examinations to explore the impacts of these factors when using Random Forest, and provides solutions to alleviate these influences with the publicly available Landsat images. Four conclusions can be drawn based on the repeatable experiments from this study. First, the performance of TOA reflectance imagery is slightly better than that of surface reflectance imagery provided by USGS in estimating fraction of impervious surface area. Second, the effect of imagery with leaf-on/off season varies, and is contingent upon different climate regions. Specifically, humid continental areas may prefer the leaf-on imagery (e.g., summer), while the tropical monsoon and Mediterranean regions seem to favor the fall and winter imagery. Third, the overall estimation performance in the humid continental area is consistently better than the other two regions in tropical monsoon and Mediterranean areas. Finally, improvements can be observed by using multi-season imagery, but the increments become less obvious when including more than two seasons. With the easy replicability of these experiments, the strategy and results of this research can improve and accommodate regional/national subpixel land cover mapping (e.g., the products of NLCD percent impervious surface and tree canopy) for large-scale environmental and climate change studies.

## References

- Adams, J.B., Smith, M.O., Johnson, P.E., 1986. Spectral mixture modeling – a new analysis of rock and soil types at the Viking Lander-1 site. *J. Geophys. Res., Solid Earth Planets* 91, 8098–8112.
- Bateson, C.A., Asner, G.P., Wessman, C.A., 2000. Endmember bundles: A new approach to incorporating endmember variability into spectral mixture analysis. *IEEE Trans. Geosci. Remote Sens.* 38 (2), 1083–1094.
- Baret, F., Weiss, M., Lacaze, R., Camacho, F., Makhmara, H., Pacholczyk, P., Smets, B., 2013. GEOV1: LAI and FAPAR essential climate variables and FCOVER global time series capitalizing over existing products. Part1: principles of development and production. *Remote Sens. Environ.* 137, 299–309.
- Belgiu, M., Drăguț, L., 2016. Random forest in remote sensing: a review of applications and future directions. *ISPRS J. Photogramm. Rem. Sens.* 114, 24–31.
- Brabec, E., Schulte, S., Richards, P.L., 2002. Impervious surfaces and water quality: a review of current literature and its implications for watershed. *J. Plann. Literat.* 16 (4), 499–514.
- Breiman, L., 2001. Random forests. *Mach. Learn.* 45, 5–32.
- Chang, C., Ji, B., 2006. Weighted abundance-constrained linear spectral mixture analysis. *IEEE Trans. Geosci. Remote Sens.* 44, 378–388.
- Coulston, J.W., Moisen, G.G., Wilson, B.T., Finco, M.V., Cohen, W.B., Brewer, C.K., 2012. Modeling percent tree canopy cover: a pilot study. *Photogramm. Eng. Rem. Sens.* 78 (7), 715–727.
- Coulston, J.W., Jacobs, D.M., King, C.R., Elmore, I.C., 2013. The influence of multi-season imagery on models of canopy cover. *Photogramm. Eng. Rem. Sens.* 79 (5), 469–477.
- Dennison, P.E., Charoensiri, K., Roberts, D.A., Peterson, S.H., Green, R.O., 2006. Wildfire temperature and land cover modeling using hyperspectral data. *Remote Sens. Environ.* 100 (2), 212–222.
- Deng, C., 2015. Incorporating endmember variability into linear unmixing of coarse resolution imagery: mapping large-scale impervious surface abundance using a hierarchically object-based spectral mixture analysis. *Rem. Sens.* 7 (7), 9205–9229.
- Deng, C., 2016. Automated construction of multiple regional libraries for neighborhood-wise local multiple endmember unmixing. *IEEE J. Sel. Top. Appl. Earth Observ. Rem. Sens.* 9 (9), 4232–4246.
- Deng, C., Wu, C., 2013a. Examining the impacts of urban biophysical compositions on surface urban heat island: a spectral unmixing and thermal mixing approach. *Rem. Sens. Environ.* 131, 262–274.
- Deng, C., Wu, C., 2013b. Estimating very high resolution urban surface temperature using a spectral unmixing and thermal mixing approach. *Int. J. Appl. Earth Obs. Geoinf.* 23, 155–164.
- Deng, C., Wu, C., 2013c. Improving small-area population estimation: an integrated geographic and demographic approach. *Ann. Assoc. Am. Geogr.* 103 (5), 1123–1141.
- Deng, C., Wu, C., 2013d. A spatially adaptive spectral mixture analysis for mapping subpixel urban impervious surface distribution. *Rem. Sens. Environ.* 133, 62–70.
- Deng, C., Wu, C., 2013e. The use of single-date MODIS imagery for estimating large-scale urban impervious surface fraction with spectral mixture analysis and machine learning techniques. *ISPRS J. Photogramm. Rem. Sens.* 86, 100–110.
- DiMiceli, C.M., Carroll, M.L., Sohlberg, R.A., Huang, C., Hansen, M.C., Townshend, J.R.G., 2011. Annual Global Automated MODIS Vegetation Continuous Fields (MOD44B) at 250 M Spatial Resolution for Data Years Beginning Day 65,

- 2000–2010, Collection 5 Percent Tree Cover. University of Maryland, College Park, MD, USA.
- Esch, T., Himmler, V., Schorcht, G., Thiel, M., Wehrmann, T., Bachofer, F., Conrad, C., Schmidt, M., Dech, S., 2009. Large-area assessment of impervious surface based on integrated analysis of single-date Landsat-7 images and geospatial vector data. *Remote Sens. Environ.* 113 (8), 1678–1690.
- Elvidge, C.D., Tuttle, B.T., Sutton, P.C., Baugh, K.E., Howard, A.T., Milesi, C., Bhaduri, B., Nemani, R., 2007. Global distribution and density of constructed impervious surfaces. *Sensors* 7 (9), 1962–1979.
- Fan, F., Fan, W., Weng, Q., 2015. Improving urban impervious surface mapping by linear spectral mixture analysis and using spectral indices. *Can. J. Rem. Sens.* 41 (6), 577–586.
- Flanagan, M., Civco, D.L., 2001. Subpixel impervious surface mapping. *Proceedings of the 2001 ASPRS Annual Convention*, St. Louis, MO, April, vol. 23.
- Frank, J., Roberts, D.A., Halligan, K., Menz, G., 2009. Hierarchical multiple endmember spectral mixture analysis (MESMA) of hyperspectral imagery for urban environments. *Remote Sens. Environ.* 113, 1712–1723.
- Guo, H., Yang, H., Sun, Z., Li, X., Wang, C., 2014. Synergistic use of optical and PolSAR imagery for urban impervious surface estimation. *Photogramm. Eng. Rem. Sens.* 80 (1), 91–102.
- Holden, C.E., Woodcock, C.E., 2016. An analysis of Landsat 7 and Landsat 8 underflight data and the implications for time series investigations. *Rem. Sens. Environ.* 185, 16–36.
- Homer, C., Huang, C., Yang, L., Wylie, B., Coan, M., 2004. Development of a 2001 National Land Cover Database for the United States. *Photogramm. Eng. Rem. Sens.* 70 (7), 829–840.
- Homer, C., Dewitz, J., Fry, J., Coan, M., Hossain, N., Larson, C., Herold, N., McKerrow, A., VanDriel, J.N., Wickham, J., 2007. Completion of the 2001 national land cover database for the conterminous United States. *Photogramm. Eng. Rem. Sens.* 73 (4), 337.
- Hu, X., Weng, Q., 2009. Estimating impervious surfaces from medium spatial resolution imagery using the self-organizing map and multi-layer perceptron neural networks. *Rem. Sens. Environ.* 113 (10), 2089–2102.
- Huang, C., Peng, Y., Lang, M., Yeo, I.Y., McCarty, G., 2014. Wetland inundation mapping and change monitoring using Landsat and airborne LiDAR data. *Rem. Sens. Environ.* 141, 231–242.
- Irish, R.R., 2000. Landsat 7 science data users handbook Report 430-15-01-003-0. National Aeronautics and Space Administration <[http://landsathandbook.gsfc.nasa.gov/pdfs/Landsat7\\_Handbook.pdf](http://landsathandbook.gsfc.nasa.gov/pdfs/Landsat7_Handbook.pdf)>.
- Jantz, P., Goetz, S.J., Jantz, C.A., 2005. Urbanization and the loss of resource lands within the Chesapeake Bay watershed. *Environ. Manage.* 36, 808–825.
- Li, G., Lu, D., Moran, E., Hetrick, S., 2013. Mapping impervious surface area in the Brazilian Amazon using Landsat Imagery. *GISci. Rem. Sens.* 50 (2), 172–183.
- Liaw, A., Wiener, M., 2002. Classification and regression by randomForest. *R News* 2 (3), 18–22.
- Luo, L., Mountrakis, G., 2010. Integrating intermediate inputs from partially classified images within a hybrid classification framework: an impervious surface estimation example. *Rem. Sens. Environ.* 114 (6), 1220–1229.
- Mejía, A.I., Moglen, G.E., 2010. Impact of the spatial distribution of imperviousness on the hydrologic response of an urbanizing basin. *Hydrol. Process.* 24 (23), 3359–3373.
- Mountrakis, G., Luo, L., 2011. Enhancing and replacing spectral information with intermediate structural inputs: a case study on impervious surface detection. *Rem. Sens. Environ.* 115 (5), 1162–1170.
- Mustard, J.F., Pieters, C.M., 1987. Quantitative abundance estimates from bidirectional reflectance measurements. *J. Geophys. Res.* 92, 617–626.
- Mustard, J.F., Pieters, C.M., 1989. Photometric phase functions of common geologic minerals and applications to quantitative-analysis of mineral mixture reflectance spectra. *J. Geophys. Res.* 10, 13619–13634.
- Myint, S.W., Okin, G.S., 2009. Modelling land-cover types using multiple endmember spectral mixture analysis in a desert city. *Int. J. Rem. Sens.* 30 (9), 2237–2257.
- Nash, D.B., Conel, J.E., 1974. Spectral reflectance systematics for mixtures of powdered hypersthene, labradorite, and ilmenite. *J. Geophys. Res.* 79, 1615–1621.
- Okujeni, A., van der Linden, S., Tits, L., Somers, B., Hostert, P., 2013. Support vector regression and synthetically mixed training data for quantifying urban land cover. *Rem. Sens. Environ.* 137, 184–197.
- Powell, R., Roberts, D.A., Hess, L., Dennison, P., 2007. Sub-pixel mapping of urban land cover using multiple endmember spectral mixture analysis: Manaus, Brazil. *Rem. Sens. Environ.* 106 (2), 253–267.
- Powell, S.L., Cohen, W.B., Yang, Z., Pierce, J.D., Alberti, M., 2008. Quantification of impervious surface in the Snohomish water resources inventory area of western Washington from 1972 to 2006. *Rem. Sens. Environ.* 112 (4), 1895–1908.
- Rashed, T., Weeks, J.R., Roberts, D., Rogan, J., Powell, R., 2003. Measuring the physical composition of urban morphology using multiple endmember spectral mixture models. *Photogramm. Eng. Rem. Sens.* 69 (9), 1011–1020.
- Reschke, J., Hüttich, C., 2014. Continuous field mapping of Mediterranean wetlands using sub-pixel spectral signatures and multi-temporal Landsat data. *Int. J. Appl. Earth Obs. Geoinf.* 28, 220–229.
- Riño, D., Chuvieco, E., Ustin, S.L., Zomer, R., Dennison, P., Roberts, D., Salas, J., 2002. Assessment of vegetation regeneration after fire through multitemporal analysis of AVIRIS images in the Santa Monica Mountains. *Rem. Sens. Environ.* 79 (1), 60–71.
- Roberts, D.A., Dennison, P.E., Gardner, M.E., Hetzel, Y., Ustin, S.L., Lee, C.T., 2003. Evaluation of the potential of Hyperion for fire danger assessment by comparison to the Airborne Visible/Infrared Imaging Spectrometer. *IEEE Trans. Geosci. Rem. Sens.* 41 (6), 1297–1310.
- Roberts, D.A., Gardner, M., Church, R., Ustin, S., Scheer, G., Green, R.O., 1998a. Mapping chaparral in the Santa Monica Mountains using multiple endmember spectral mixture models. *Rem. Sens. Environ.* 65, 267–279.
- Roberts, D.A., Quattrochi, D.A., Hulley, G.C., Hook, S.J., Green, R.O., 2012. Synergies between VSWIR and TIR data for the urban environment: an evaluation of the potential for the hyperspectral infrared imager (HypSIIRI) decadal survey mission. *Rem. Sens. Environ.* 117, 83–101.
- Roberts, D.A., Regelbrugge, J., Pedreros, D., Ustin, S.L., 1998b. Mapping the distribution of wildfire fuels using AVIRIS in the Santa Monica Mountains. NASA Report.
- Roy, D.P., Kovalsky, V., Zhang, H.K., Vermote, E.F., Yan, L., Kumar, S.S., Egorov, A., 2016. Characterization of Landsat-7 to Landsat-8 reflective wavelength and normalized difference vegetation index continuity. *Rem. Sens. Environ.* 185, 57–70.
- Scott, D., Petropoulos, G.P., Moxley, J., Malcolm, H., 2014. Quantifying the physical composition of urban Morphology throughout Wales based on the time series (1989–2011) analysis of Landsat TM/ETM+ images and supporting GIS data. *Rem. Sens.* 6 (12), 11731–11752.
- Sexton, J.O., Song, X.P., Feng, M., Noojipady, P., Anand, A., Huang, C., Kim, D.H., Collins, K.M., Channan, S., Townshend, J.R., 2013. Global, 30-m resolution continuous fields of tree cover: Landsat-based rescaling of MODIS vegetation continuous fields with lidar-based estimates of error. *Int. J. Digital Earth* 6 (5), 427–448.
- Schmidt, G., Jenkerson, C., Masek, J., Vermote, E., Gao, F., 2013. Landsat Ecosystem Disturbance Adaptive Processing System (LEDAPS) Algorithm Description (No. 2013-1057). US Geological Survey.
- Shao, Y., Lunetta, R.S., 2011. Sub-pixel mapping of tree canopy, impervious surfaces, and cropland in the Laurentian Great Lakes Basin using MODIS time-series data. *IEEE J. Sel. Top. Appl. Earth Observ. Rem. Sens.* 4 (2), 336–347.
- Shi, C., Wang, L., 2014. Incorporating spatial information in spectral unmixing: a review. *Rem. Sens. Environ.* 149, 70–87.
- Somers, B., Delalieux, S., Stuckens, J., Verstraeten, W.W., Coppin, P., 2009. A weighted linear spectral mixture analysis approach to address endmember variability in agricultural production systems. *Int. J. Rem. Sens.* 30, 139–147.
- Song, C., Woodcock, C.E., Seto, K.C., Lenney, M.P., Macomber, S.A., 2001. Classification and change detection using Landsat TM data: when and how to correct atmospheric effects? *Rem. Sens. Environ.* 75 (2), 230–244.
- Suganuma, H., Abe, Y., Taniguchi, M., Tanouchi, H., Utsugi, H., Kojima, T., Yamada, K., 2006. Stand biomass estimation method by canopy coverage for application to remote sensing in an arid area of Western Australia. *For. Ecol. Manage.* 222 (1), 75–87.
- Sung, C.Y., Li, M.H., 2012. Considering plant phenology for improving the accuracy of urban impervious surface mapping in a subtropical climate regions. *Int. J. Rem. Sens.* 33 (1), 261–275.
- Thorp, K.R., French, A.N., Rango, A., 2013. Effect of image spatial and spectral characteristics on mapping semi-arid rangeland vegetation using multiple endmember spectral mixture analysis (MESMA). *Rem. Sens. Environ.* 132, 120–130.
- Tsutsumida, N., Comber, A., Barrett, K., Saizen, I., Rustiadi, E., 2016. Sub-pixel classification of modis evi for annual mappings of impervious surface areas. *Rem. Sens.* 8 (2), 143.
- United Nations Environment Program, 2010. Africa Water Atlas Retrieved from: <[http://www.unep.org/pdf/africa\\_water\\_atlas.pdf](http://www.unep.org/pdf/africa_water_atlas.pdf)>.
- U.S. Geological Survey, 2016a. Landsat 8 (L8) data users handbook Retrieved from: <<https://landsat.usgs.gov/sites/default/files/documents/Landsat8DataUsersHandbook.pdf>>.
- U.S. Geological Survey, 2016b. Provisional Landsat 8 Surface Reflectance Code Product Guide Retrieved from: <[https://landsat.usgs.gov/sites/default/files/documents/provisional\\_lasrc\\_product\\_guide.pdf](https://landsat.usgs.gov/sites/default/files/documents/provisional_lasrc_product_guide.pdf)>.
- Walton, J., 2008. Subpixel urban land cover estimation: comparing Cubist, Random Forests, and support vector regression. *Photogramm. Eng. Rem. Sens.* 74 (10), 1213–1222.
- Wang, L., Shi, C., Diao, C., Ji, W., Yin, D., 2016. A survey of methods incorporating spatial information in image classification and spectral unmixing. *Int. J. Rem. Sens.* 37 (16), 3870–3910.
- Wetherley, E.B., Roberts, D.A., McFadden, J.P., 2017. Mapping spectrally similar urban materials at sub-pixel scales. *Remote Sens. Environ.* 195, 170–183.
- Weng, Q., 2012. Remote sensing of impervious surfaces in the urban areas: requirements, methods, and trends. *Rem. Sens. Environ.* 117, 34–49.
- Weng, Q., Hu, X., 2008. Medium spatial resolution satellite imagery for estimating and mapping urban impervious surfaces using LSMA and ANN. *IEEE Trans. Geosci. Rem. Sens.* 46 (8), 2397–2406.
- Weng, Q., Hu, X., Liu, H., 2009. Estimating impervious surfaces using linear spectral mixture analysis with multitemporal ASTER images. *Int. J. Rem. Sens.* 30 (18), 4807–4830.
- White, M.D., Greer, K.A., 2006. The effects of watershed urbanization on the stream hydrology and riparian vegetation of Los Peñasquitos Creek, California. *Landscape Urban Plan* 74, 125–138.
- Wu, C., 2004. Normalized spectral mixture analysis for monitoring urban composition using ETM+ imagery. *Remote Sens. Environ.* 93 (4), 480–492.
- Wu, C., Yuan, F., 2007. Seasonal sensitivity analysis of impervious surface estimation with satellite imagery. *Photogramm. Eng. Rem. Sens.* 73 (12), 1393–1401.

- Xian, G., Crane, M., Su, J., 2007. An analysis of urban development and its environmental impact on the Tampa Bay watershed. *J. Environ. Manage.* 85 (4), 965–976.
- Xian, G., Homer, C., Meyer, D., Granneman, B., 2013. An approach for characterizing the distribution of shrubland ecosystem components as continuous fields as part of NLCD. *ISPRS J. Photogramm. Rem. Sens.* 86, 136–149.
- Xian, G., Homer, C., Rigge, M., Shi, H., Meyer, D., 2015. Characterization of shrubland ecosystem components as continuous fields in the northwest United States. *Rem. Sens. Environ.* 168, 286–300.
- Xiao, R.B., Ouyang, Z.Y., Zheng, H., Li, W.F., Schienke, E.W., Wang, X.K., 2007. Spatial pattern of impervious surfaces and their impacts on land surface temperature in Beijing, China. *J. Environ. Sci.* 19 (2), 250–256.
- Yang, L., Huang, C., Homer, C., Wylie, B., Coan, M., 2003. An approach for mapping large-area impervious surface: synergistic use of Landsat 7 ETM+ and high spatial resolution imagery. *Can. J. Rem. Sens.* 29, 230–240.
- Yang, F., Matsushita, B., Fukushima, T., Yang, W., 2012. Temporal mixture analysis for estimating impervious surface area from multi-temporal MODIS NDVI data in Japan. *ISPRS J. Photogramm. Rem. Sens.* 72, 90–98.
- Yu, D., Wu, C., 2004. Understanding population segregation from Landsat ETM+ imagery: a geographically weighted regression approach. *GISci. Rem. Sens.* 41 (3), 187–206.
- Yuan, F., Bauer, M.E., 2007. Comparison of impervious surface area and normalized difference vegetation index as indicators of surface urban heat island effects in Landsat imagery. *Rem. Sens. Environ.* 106, 375–386.
- Zhang, J., Rivard, B., Sanchez-Azofeifa, A., 2005. Spectral unmixing of normalized reflectance data for the deconvolution of lichen and rock mixtures. *Rem. Sens. Environ.* 95, 57–66.
- Zhang, J., Rivard, B., Sanchez-Azofeifa, A., Castro-Esau, K., 2006. Intra- and inter-class spectral variability of tropical tree species at La Selva, Costa Rica: implications for species identification using HYDICE imagery. *Rem. Sens. Environ.* 105, 129–141.
- Zhang, Z., Liu, C., Luo, J., Shen, Z., Shao, Z., 2015. Applying spectral mixture analysis for large-scale sub-pixel impervious cover estimation based on neighbourhood-specific endmember signature generation. *Rem. Sens. Lett.* 6 (1), 1–10.
- Zhang, H., Lin, H., Li, Y., Zhang, Y., Fang, C., 2016. Mapping urban impervious surface with dual-polarimetric SAR data: an improved method. *Landscape Urban Plann.* 151, 55–63.
- Zhang, H., Zhang, Y., Lin, H., 2012. A comparison study of impervious surfaces estimation using optical and SAR remote sensing images. *Int. J. Appl. Earth Obs. Geoinf.* 18, 148–156.
- Zhang, H., Zhang, Y., Lin, H., 2014. Seasonal effects of impervious surface estimation in subtropical monsoon regions. *Int. J. Digital Earth* 7 (9), 746–760.
- Zhou, B., He, H.S., Nigh, T.A., Schulz, J.H., 2012. Mapping and analyzing change of impervious surface for two decades using multi-temporal Landsat imagery in Missouri. *Int. J. Appl. Earth Obs. Geoinf.* 18, 195–206.
- Zhou, Y., Wang, Y., Gold, A.J., August, P.V., 2010. Modeling watershed rainfall–runoff relations using impervious surface–area data with high spatial resolution. *Hydrogeol. J.* 18 (6), 1413–1423.
- Zhu, Z., Wang, S., Woodcock, C.E., 2015. Improvement and expansion of the Fmask algorithm: Cloud, cloud shadow, and snow detection for Landsats 4–7, 8, and Sentinel 2 images. *Rem. Sens. Environ.* 159, 269–277.
- Zhu, Z., Woodcock, C.E., 2012. Object-based cloud and cloud shadow detection in Landsat imagery. *Rem. Sens. Environ.* 118, 83–94.
- Zhu, Z., Fu, Y., Woodcock, C.E., Olofsson, P., Vogelmann, J.E., Holden, C., Wang, M., Dai, S., Yu, Y., 2016. Including land cover change in analysis of greenness trends using all available Landsat 5, 7, and 8 images: a case study from Guangzhou, China (2000–2014). *Rem. Sens. Environ.* 185, 243–257.